Journal of
Materials Chemistry A

ROYAL SOCIETY
OF CHEMISTRY

COMMUNICATION

View Article Online
View Journal

Check for updates

Cite this: DOI: 10.1039/d5ta08284f

Mobility of interfaces in silicon-based anodes

Heesoo Park * and Alexey Y. Koposov *

Received 11th October 2025
Accepted 4th December 2025

DOI: 10.1039/d5ta08284f

rsc.li/materials-a

Silicon (Si) is a promising anode material for next-generation lithium-ion batteries (LIBs), but its practical use is limited due to severe degradation during electrochemical cycling. The morphological changes of Si are affected by the selection of an electrolyte, and its role in such transformations remains a subject of debate. The lack of experimental and computational methods to examine these interactions at the molecular level also impedes the accurate chemical characterization of this complex system. This study evaluates the interaction of Si nanoparticle(s) with ether-based electrolytes using a reactive force field approach. The interplay between the Si nanoparticles and the electrolyte during (de)lithiation leads to a significant structural deformation of the Si particles and the formation of a thick interdiffusion layer where Si atoms are mixed with the electrolyte moieties. This layer is mainly formed during delithiation, whereas lithiation leads to constrained interdiffusion. The intermixing and mobility at the Si/electrolyte interface highlight the electrolyte's critical role in mitigating the degradation of Si-based anodes during delithiation.

1 Introduction

The poor structural stability of an active material in lithium-ion batteries (LIBs) typically leads to rapid deterioration of the electrochemical performance through repeated charge and discharge cycles, limiting its practical implementation. Many materials whose structural integrity is not compromised through electrochemical cycling have become state-of-the-art for modern LIBs. For instance, the achievements of graphite as an anode material in LIBs are often attributed to its remarkable structural stability, and therefore long lifespan.[1] However, the continued demand for improving the energy density of LIBs has driven research into advanced active materials with capacities higher than that of graphite, leading to a significant diversification in battery chemistry, often at the cost of reduced stability.[2,3]

Among the various active materials introduced to replace graphite, silicon (Si) stands out as the most promising candidate for next-generation anodes in LIBs. Si has a theoretical gravimetric capacity of 3579 mAh g^{-1} when fully lithiated to $Li_{15}Si_4$.[4–6] The high capacity of Si-based anodes is realized *via* an alloying reaction during charge, while the dealloying process occurs during discharge. As a result, unlike the intercalation process in graphite that maintains the layered structure, the transformations in lithiated Si (Li_xSi) involve not only morphological changes of the active particles, but also breaking and formation of multiple chemical bonds.

To minimize the effect of large expansion/contraction of Si during electrochemical cycling, Si nanoparticles (NPs) were introduced more than a decade ago, but their practical use is limited.[7] Multiple efforts have focused on combining Si with other materials, such as Si-containing composites,[6–10] or elements which resulted in a family of substoichiometric compounds such as SiN_x and SiO_x.[11–14] Alternatively, specially designed polymers can be incorporated into a Si-based electrode as binders to maintain the structural integrity of the active material.[7,15–17] Despite efforts, controlling the degradation of Si-based anodes remains challenging due to limited understanding of the molecular interactions at the electrode–electrolyte interface, complicated by deformation layers,[16,18–21] as well as the interaction between Si atoms and Li ions during the chemical and structural transformations of Li_xSi.[6,22–25]

The present study investigates the chemical interplay between Si NPs and electrolyte molecules during lithiation and subsequent delithiation, with a particular focus on ether-based electrolytes. Two ethers were selected as electrolytes: polyethylene oxide (PEO) – one of the most common polymer electrolytes,[26,27] and dimethoxyethane (DME) – a liquid electrolyte shown to improve the electrochemical performance of multiple anode materials.[28–30] We discuss how irreversible intrusion of Si into the electrolyte diminishes the mobile conductive phase at

---

Centre for Materials Science and Nanotechnology, Department of Chemistry, University of Oslo, 0371 Oslo, Norway. E-mail: heesoo.park@smn.uio.no; alexey.koposov@kjemi.uio.no

the interface, which could potentially impair the performance of Si-based anodes.

2 Molecular dynamics modeling of interfaces

Reactive force field (ReaxFF) coupled with the grand canonical Monte Carlo method (ReaxFF-GCMC)[31,32] was used to examine the migration of Li across the active particle/electrolyte interface,[33] as implemented in LAMMPS.[34,35] ReaxFF MD simulations effectively model chemical interactions within materials during chemical transformations associated with (de)lithiation.,[36–39] while the GCMC method facilitates the modeling of Li accumulation behavior around active materials.[32,40]

The majority of studies of active material evolution at the interface in modeling typically adopts a flat surface model,[21] where only the top of the simulation box is exposed to the environment. This flat surface does not necessarily reflect the real chemical system since uniaxial expansion of the Li_xSi phase during lithiation can induce shear stress, which can lead to fractures.[41–43] Therefore, to better account for the expansion of Si in all dimensions, we have constructed spherical Si NPs with a diameter of 23 Å consisting of 348 Si atoms, which represents a reasonable compromise between the particle size and modeling capabilities. Such amorphous Si particles are often used experimentally to alleviate the stress associated with expansion.[44] Furthermore, the spherical interface boundaries enhance interactions with the electrolyte by providing conformational options greater than those of flat surfaces. A flat interface can restrict the mobility of PEO polymer chains.[45–47] We defined a 1.5 Å thick shell for the Li insertion region above the Li_xSi surface to precisely position Li between the electrolyte and the active material (Fig. 1).

The amorphous Si NPs, after being quenched from 1700 K to 300 K over 40 ps at 1 atm, were encapsulated in the electrolyte using either PEO or DME. Both electrolytes are ether-based compounds and have demonstrated promising results with Si-based anodes in LIBs.[28,48,49] While carbonate-based electrolytes are typically used for Si-based electrodes, recent developments indicate that the use of other electrolyte systems may affect their cyclability. DME is a small molecule with the formula of $C_4H_{10}O_2$, featuring two methoxy groups attached to an ethylene backbone, while PEO is a macromolecular polymer made up of repeating ethylene oxide units, resulting in a long-chain structure. PEO represents one of the most studied polymer systems for incorporation with Si-based materials.[26,27] Consequently, the long chains of PEO are expected to influence the physical and mechanical properties, especially at the interface. These alterations in chemical interactions at the interface can influence the formation of Si–Si bonds in the NPs, with the inclusion of Li, which in turn could change electrochemical performance during cycling.[50–52]

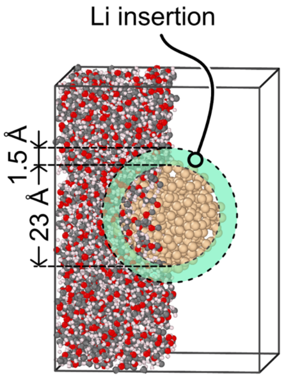

Fig. 1 Schematic illustrations of the simulation box are illustrated as follows: a spherical Si-based particle is encased in PEO. One half of the region containing PEO is omitted for clarity. The spheres are color-coded: gray (carbon), red (oxygen), white (hydrogen), and brown (silicon). The lithium insertion region, as determined by the GCMC, is highlighted in light green.

MD simulations were carried out at 350 K, since PEO-based batteries show optimal operation at this temperature.[26,27] The force field provides the experimental characteristics, including the temperature-dependent density of PEO and the voltage profile of Si, as shown in Fig. S2–S3 in the SI. Upon lithiation, there are two phases of lithiation of Si and their boundary migration velocity was estimated to be constant (0.06 nm s^{-1}).[23,53–55] This two-phase mechanism occurs because the lithiation rates differ between the a-$Li_{2.5}Si$ and a-$Li_{3.75}Si$ phases. However, in this study only a single Li diffusion phase in the amorphous a-Li_xSi alloy was observed during simulations, due to the relatively low Li concentration in the Si NPs.

It is well established that a solid-electrolyte interphase (SEI) composed of various organic and inorganic components develops during the electrochemical cycling.[56,57] The chemical structure of the SEI is extremely complex, which substantially complicates the modeling of this system as a whole at the atomistic level. However, during the expansion/contraction of Si NPs, the SEI is often detached from the surface of a particle, constantly exposing new Si surfaces to the electrolyte. Therefore, the electrolyte properties will strongly affect the direct interaction between the active material and the electrolyte during (de)lithiation.

3 Results and discussion

The chemical system in the lithiation was regulated by manipulating the external chemical potential (μ) of the ideal gas reservoir in the GCMC scheme. Fig. 2a and b illustrate the evolution of specific capacity for Si NPs in PEO (panel a) and DME (panel b) with various chemical potentials (μ). At $\mu = -10$ kcal mol^{-1}, a notable buildup of Li was observed on the particle surface as the Li content in Li_xSi increased. Moreover, the Si NPs in DME underwent notable deformation. However, altering the chemical potential within the examined range of $\mu = -15$ to -27 kcal mol^{-1} (see Fig. S4 in the SI) had a negligible effect on the structure of the lithiated Li_xSi NPs. In particular, a specific capacity over 2000 mAh g^{-1} was achieved at $\mu = -15$ kcal mol^{-1} for both PEO and DME. For specific capacities exceeding approximately 2300 mAh g^{-1} ($x > 2.4$ in Li_xSi), the GCMC scheme shows a significant reduction in Li insertion at the

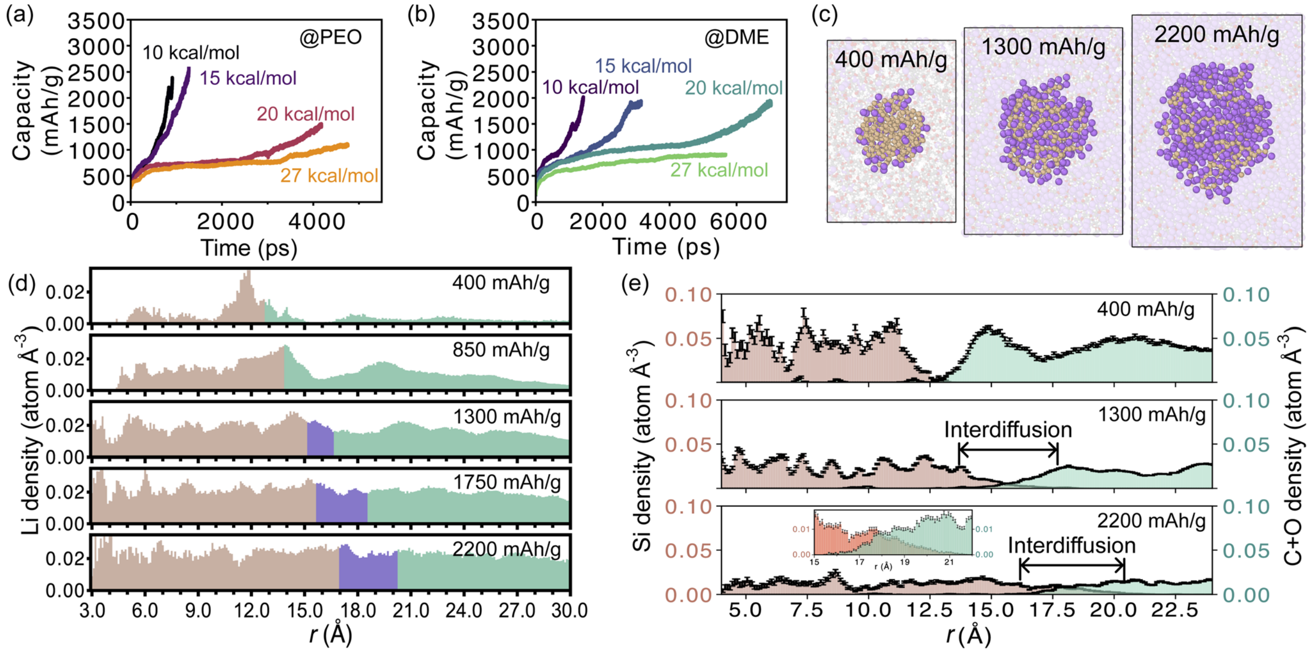

Fig. 2 Specific capacity of Si NPs in (a) PEO and (b) DME. (c) Snapshots of cross-sections of the simulation cell with lithiated Si NPs in PEO. Li (purple) and Si (brown) of Li_xSi are highlighted. (d) Li densities of Si–PEO as a function of radial distance with respect to the center of mass of the Si NPs. Color codes are: Si region (brown), Si–PEO interdiffusion region (purple), and PEO region (green) (e) number densities of silicon (Si, brown) within the Si NPs, and carbon and oxygen (C + O, green) in PEO as a function of radial distance.

interface region as only a few Li atoms were inserted over a duration longer than 500 ps.

The μ value was set to accelerate lithiation, even though the chemical potential exceeds the calculated Li formation energy of -23.6 kcal mol^{-1}. Upon lithiation, the Li content was determined by counting the Li atoms forming covalent bonds with Si atoms in the NP structure, while we could observe the volumetric expansion of Si NPs, as shown in Fig. 2c.

Fig. 2d presents the Li density profile, highlighting the crucial role of Li accumulation in the compositional transition process. Incorporation of Li into the Li_xSi structure involves a critical step known as desolvation, which refers to the extraction of Li from the surrounding PEO chains or DME molecules. This process is essential for effective lithiation of NPs, as it frees Li to be available for insertion into the Li_xSi structure.[58,59] After desolvation, Li diffuses through Li_xSi.[25]

Li diffusivity in Li_xSi is generally lower (ranging from 10^{-14} to 10^{-10} cm^2 s^{-1})[60–62] than that in the electrolyte; in DME, Li diffusivity can range between 10^{-5} and 10^{-6} cm^2 s^{-1},[29,63] while in PEO, it spans from 10^{-7} to 10^{-8} cm^2 s^{-1}.[26,27] As a result, the concentration of Li in the PEO phase increases, driven by the high concentration of Li and diffusion at the interface. The elevated concentration of Li within the polymer signifies notable resistance in the desolvation process of Li that transitions from the PEO phase into Li_xSi NPs. This observation is corroborated with experimental evidence that Li concentration may increase in the electrolyte at the reaction boundary, forming a nanoscale layer.[23,64,65]

The Li insertion at the end of the lithiation simulations was reduced because of limited Li diffusion within Si NPs and desolvation in the electrolyte as the concentration of Li rises. When comparing Si NPs encapsulated within PEO or DME, we observed that the maximum achievable specific capacity of Li_xSi in DME was comparatively lower, reaching only 2000 mAh g^{-1}. This variation suggests that the desolvation of Li at the Li_xSi/PEO interface is faster in the polymer than in DME, thereby affecting the kinetics of Li_xSi lithiation. In addition, while comparing the number of Li within the Li_xSi particles *versus* those in the electrolyte, we observed that during lithiation, Li transferred more effectively into the Si particle region from PEO than from DME, as shown in Fig. S7 in the SI.

The atomic distribution in the Li_xSi and electrolyte regions was assessed by counting the Si atoms of Li_xSi and the C and O atoms of PEO as a function of lithiation. This compositional radial distribution is represented by the densities of the atoms as shown in Fig. 2e. The Si atoms in the expanding Li_xSi phase migrated outward, resulting in volume expansion as the lithiation of Li_xSi progresses. This expansion also initiated the interdiffusion of Si atoms with the chains of PEO leading to the formation of a thin layer (approximately 4 Å in thickness) where Si atoms and PEO chains were intermixed. The formation of such a layer facilitated the transfer of Li across the interface. Similarly, the interdiffusion layer appeared between Si atoms and DME molecules, as illustrated in Fig. S4 in the SI. This observation suggests that both PEO and DME affect interdiffusion during the lithiation process, except for an abrupt structural alteration between 700 and 800 mAh g^{-1} due to the formation of Si fragments in DME. This structural alteration is evidenced by the root-mean-square distance (RMSD) of Si atoms in Fig. S5 and S6 in the SI using pristine Si NPs as a reference.

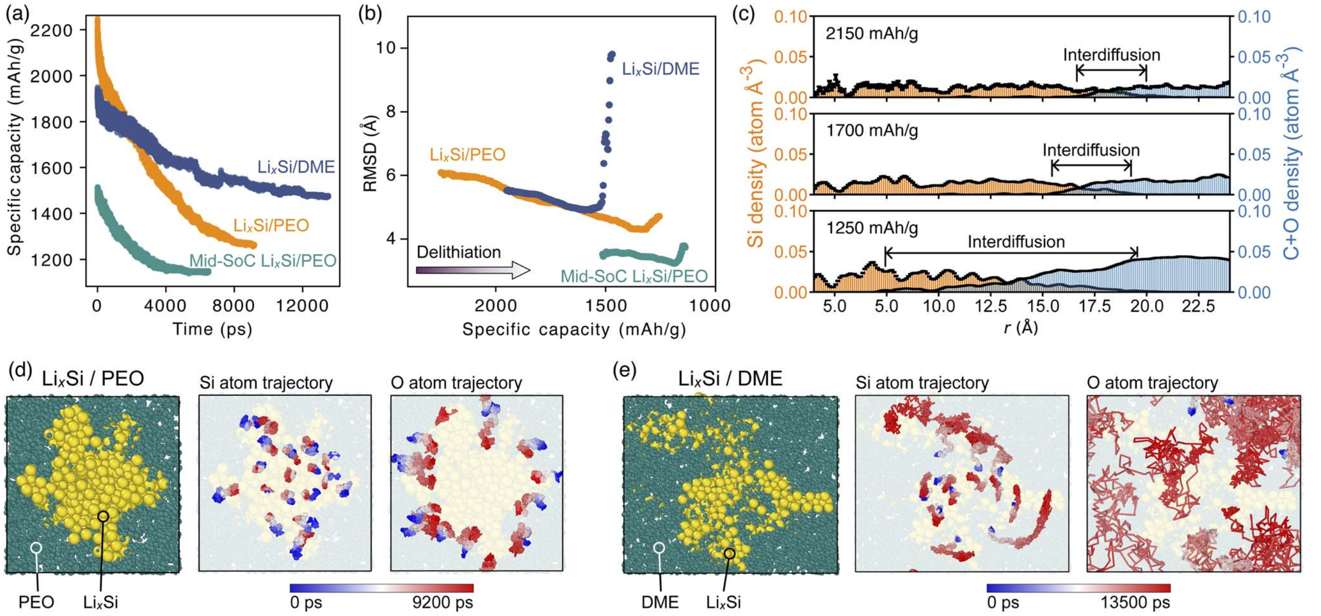

Fig. 3 (a) Specific capacity of Li_xSi NPs in PEO and DME in the delithiation processes. (b) RMSD of the positions of the Si atoms as a function of the specific capacity. (c) Number densities of Si (orange) within the Si NPs, and carbon and oxygen (C + O, blue) in PEO as a function of radial distance with respect to the center of mass of the Si NP. Delithiated structures and the trajectory lines of the selected atoms of (d) Li_xSi/PEO and (e) Li_xSi/DME. In the left panel, the areas with Li_xSi are highlighted in yellow, while the electrolyte areas are shown in green. The middle panel depicts the trajectory lines of selected Si atoms, while the right panel shows the corresponding O atoms in PEO and DME. The red–white–blue color of trajectory lines represents the simulation time.

After examining lithiated structures, the MD simulations of consecutive delithiation were performed using the structures that were formed during the lithiation simulations at $\mu = -15$ kcal mol^{-1}. In addition to the Si NPs lithiated in PEO (Li_xSi/PEO) and DME (Li_xSi/DME), we also examined the partially lithiated Li_xSi particle in PEO, where lithiation was stopped at the intermediate state corresponding to 1500 mAh g^{-1} (Mid-SoC Li_xSi/PEO). This delithiation process was done to compare the deformation of the Si NPs as a function of the degree of lithiation. Fig. 3a presents the delithiation process of the Si NPs. Unlike lithiation, the progression of delithiation in Li_xSi NPs was found to be strongly dependent on the electrolyte.

Theoretical studies of the thermodynamic characteristics for Li_xSi have shown that the removal of Li (dealloying) is less favorable than the addition of Li (alloying) when $x < 2$ (which corresponds to a specific capacity below 1909 mAh g^{-1}), as the formation of Li–Si bonds contributes to the thermodynamic stability of the material.[66–70] This thermodynamic behavior indicates a decline in Li extraction as delithiation continues. Additionally, it highlights the electrolyte's role to assist with the Li extraction at the interface by dissolving Li at the interface. To evaluate electrolyte effects, we conducted delithiation simulations until no Li extraction from Li_xSi NPs was occurring over the simulation of 300 ps and examined the evolution of the corresponding specific capacities.

The specific capacity decreases more gradually during delithiation when the Si NPs are placed in DME: a more significant decline in the specific capacity in PEO was observed. The similar decline in specific capacity for Mid-SoC Li_xSi/PEO indicates that the initial state of lithiation does not affect the rate of delithiation. As a result, the delithiated Li_xSi NPs in PEO demonstrated a specific capacity lower than that of Li_xSi NPs delithiated in DME. This indicates a significant amount of trapped Li in the particles.

Notable deformation of Si NPs was observed during delithiation in both PEO and DME, with Si atom movements being analyzed using RMSD calculations, as shown in Fig. 3b. The RMSD values indicate that the volume of Si NPs initially decreased during delithiation, leading to the structure of Li_xSi clusters with low Li content. However, as the delithiation continues, the particles started to disintegrate. Specifically, during the later phase of delithiation, Li–Si segments permeated the region containing chains of PEO and DME molecules, while the movement of electrolyte moieties into the Li_xSi interior was also observed. This interdiffusion across the interface for PEO as an electrolyte is illustrated in Fig. 3c, where the atomic occupation of each region is assessed by the number densities for Si atoms of Li_xSi and C and O atoms of PEO. The interdiffusion length was initially estimated to be approximately 4 Å, however, during delithiation it extended to about 13 Å as Li diffusion and extraction led to substantial atomic mixing.

The degree to which Si NPs undergo deformation was especially severe for Li_xSi/DME, as the RSMD values showed a significant increase at 1500 mAh g^{-1}, contrasting with those observed for Li_xSi/PEO. This remarkable difference originates from the greater dispersion of Si atoms in DME than in PEO. Fig. 3d displays the restricted dispersion of Li_xSi fragments in

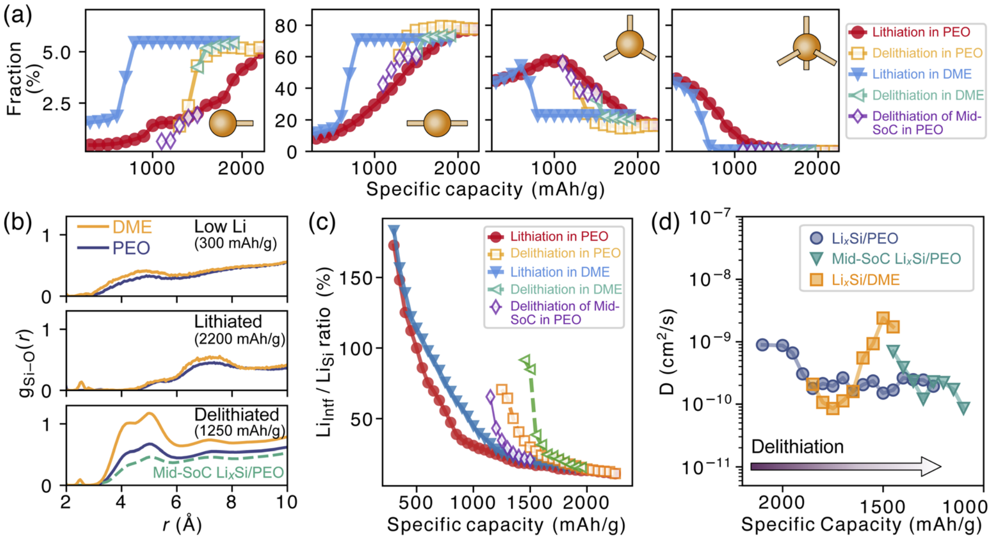

Fig. 4 (a) Fraction of the Si atoms of two-, three-, four-fold coordinated. (b) Radial distribution function between Si and O atoms. (c) Ratio of Li at the interface to the Li content within Li$_x$Si. (d) Calculated Li diffusion coefficient as a function of specific capacity during the delithiation process.

PEO, as indicated by the trajectory lines of selected atoms,[71] contrasting with the extensive intermixing observed in DME shown in Fig. 3e. The polymeric nature of PEO efficiently constrains the deformation of Si NPs by preventing the migration of PEO segments toward Si NPs and, thus, hindering the movement of Si atoms towards the PEO region. As expected, the movement of DME molecules is unimpeded due to the absence of chain constraints, leading to intermixing of two phases. In addition, the void space autocorrelation function (Fig. S8 in the SI) demonstrates that the void space dissipates at a higher rate in DME compared to PEO: DME molecules rapidly fill the nearby vacancies created by Li movement.

The adhesion energy between Si particles and electrolytes increased during lithiation and delithiation, due to the inserted Li enhancing non-bonded interactions (see Fig. S9 in the SI). This increasing adhesion energy led to greater coherence in structural changes and increased intermixing between the particle and electrolyte regions. Meanwhile, the non-bonded interactions of the pristine Si particles with PEO and DME indicate that PEO is more loosely bonded to the Si atoms. This weaker binding may allow Li to adsorb onto the surface of Si particles by substituting the PEO chains, enhancing integration between the Si NPs and Li. Moreover, the similar strength of non-bonded interactions indicates that the limited intermixing of Si/PEO during delithiation results from the kinetic constraints on the segmental motion, unlike the more mobile DME molecules.

During the delithiation phase, multiple interactions take place in the system: PEO chains and DME molecules engage in solvation of the extracted Li atoms *via* interactions with ether oxygens; dealloyed Si atoms tend to reform Si–Si bonds. However, PEO and DME can impede this structural reconstruction of Si NPs by interacting with the dealloyed Si atoms in the interdiffusion layer. Therefore, the influence of intermixing on delithiation can be examined by analysis of reestablished Si–Si bonds in the Li$_x$Si NPs. This analysis was carried out by determining the coordination number of Si atoms in relation to their adjacent Si atoms, as shown in Fig. 4a.

During lithiation, the increase in the number of single- and two-fold coordinated Si atoms, along with the decrease in the number of three- and four-fold coordinated Si atoms, indicates that Si NPs break into Si–Si chain segments. In particular, as the specific capacity varies from 600 to 800 mAh g^{-1} in the case of DME, there is a notable rise in single- and two-fold coordinated Si atoms. As a result, Si NPs are fragmented into shorter Si–Si chains when DME was selected as an electrolyte compared to PEO at equivalent Li concentrations.

During the delithiation of Li$_x$Si/PEO NPs, the number of three-fold coordinated Si–Si bonds increased, while the number of single- and two-fold coordinated Si bonds decreased, indicating Si–Si restructuring. However, the number of four-fold coordinated Si bonds remained unchanged. Similarly, in the coordination analysis of the delithiated Li$_x$Si/DME and Mid-SoC Li$_x$Si/PEO NPs, an increase in the proportion of three-fold coordinated Si atoms was observed, with no four-fold coordinated Si atoms observed during the simulations.

This observation of four-fold coordinated Si atoms aligns with the loss of the Si–Si bond reformation tendency in the interdiffusion layer. Fig. 4b displays the radial distribution function by the histogram of the distances between the Si and O atoms in Li$_x$Si and the associated electrolyte, respectively. The distance increased from 4.8 Å to 7.3 Å during Li insertion both in PEO and DME, as Li atoms accumulated at the interfaces. In the consecutive delithiation process, the increase in intensity of the main peaks (4–5 Å) indicates that there are more surrounding ether groups near the Li$_x$Si segments compared to Li$_x$Si NPs with low Li concentration. The interdiffusion layer hinders the kinetics required to reorganize a dense Si–Si bond network; with this tendency being more pronounced in the case of DME as the electrolyte.

Fig. 4c illustrates that the concentration of Li at the interface, compared to the interior of Li_xSi, reveals changes in Li distribution associated with Si–Si reconstruction and Si–PEO and Si–DME interdiffusion. We defined the Li atoms at the interface (Li_{Intf}) as those located between the outer Si atoms of Li_xSi and the constituent atoms of PEO and DME. Meanwhile, Li atoms that are coordinated with Si atoms are referred to as Li_{Si}.

The relative amount of Li_{Intf}, which exceeds 100%, indicates that more Li atoms accumulate above the surface of Li_xSi than within the NPs during the initial lithiation process. The accumulation resulted in the formation of lithiated Li_xSi, with Li diffusing internally, and the ratio decreased as Li_xSi involved a higher Li concentration. During the delithiation process, a notable phenomenon occurred in which Li accumulated at the interface, while Li_{Intf} reached levels exceeding 70%. Considering the changes in distances between the Si atom and the electrolyte discussed above, the substantial accumulation suggests an obstruction to the migration of Li into the electrolyte bulk within the interdiffusion layer. Owing to the polymeric structure of PEO, its constrained intermixing facilitated Li transfer at the interface until the specific capacity went under 1500 mAh g^{-1}, differing from DME molecules in the interdiffusion layer. The lithiation level of Mid-SoC Li_xSi/PEO was linked to Li accumulation near the interface at a lowered specific capacity, however, it did not improve the restoration of the Si NP structure.

The decrease in Li transfer during delithiation is primarily attributed to significant interdiffusion, which played a crucial role in the observed changes. The Li diffusivity measured during the delithiation process varied, as shown in Fig. 4d. An unexpected increase in diffusivity was observed due to the disintegration of Li_xSi fragments in DME, which allowed Li to move along with these fragments. However, the overall trend showed a decrease in Li diffusivity as the interdiffusion thickens. Consequently, this impeded transport could have implications for the overall efficiency of lithium extraction, highlighting the importance of understanding these interfacial dynamics in alloying-type anode performance.

4 Conclusions

In summary, the modeling of the interfaces between Si NPs and ether-based electrolytes revealed that significant deformation of Si nanoparticles occurs during the delithiation process, accompanied by a thickening interdiffusion layer, whereas Li insertion does not result in notable deformation. The polymer structure of PEO mitigates intermingling with the Li_xSi segments and promotes the three-fold coordinated Si to adhere to a similar trajectory, ultimately leading to the delithiation in Si nanoparticles. In contrast, for Li_xSi in DME, the surface of delithiated Si nanoparticles disassembles, leading to the interdiffusion of Li_xSi with the surrounding DME molecules, hindering Si–Si reconstruction. The diminished degree of atomic intermixing during the delithiation process with PEO demonstrates the importance of the electrolyte in alleviating the deformation of Si nanoparticles.

Our results highlight the chemomechanical interactions between the active material and electrolyte molecules, leading to structural variations during the cycles. Although small particles in this study lack phenomena seen in larger particles, such as the presence of two lithiated phases and phase migration, they effectively provide key insights into interface behavior in batteries, especially for the Si atoms near the subsurface of larger particles. Polymers, in particular, demonstrate a reduced level of element mixing during delithiation, suggesting that restricted movement within the interdiffusion layer is the key to mitigating the structural disintegration of Si-based anodes.

Author contributions

A. Y. K. conceived the study and supervised the project. H. P. performed the model building, MD simulations, post-process calculations, and data curation. H. P. and A. Y. K. contributed to the analysis, data interpretation, and manuscript writing.

Conflicts of interest

The authors declare that they have no competing interests.

Data availability

The data related to the current findings are included as the supplementary information (SI). Supplementary information is available. See DOI: https://doi.org/10.1039/d5ta08284f.

Acknowledgements

The authors acknowledge the SALAMANDER project funded by the European Union's Horizon Europe research and innovation programme under grant agreement No. 101104028 and 101104022 (BATTERY 2030+ CSA3). The authors acknowledge the Research Council of Norway for providing computer time (under the project numbers NN2875k and NS2875k) at the Norwegian supercomputer facility.

References

1 J. Betz, G. Bieker, P. Meister, T. Placke, M. Winter and R. Schmuch, *Adv. Energy Mater.*, 2019, **9**, 1803170.
2 C. Wölke, B. A. Sadeghi, G. G. Eshetu, E. Figgemeier, M. Winter and I. Cekic-Laskovic, *Adv. Mater. Interfaces*, 2022, **9**, 2101898.
3 T. Placke, R. Kloepsch, S. Dühnen and M. Winter, *J. Solid State Electrochem.*, 2017, **21**, 1939–1964.
4 T. M. Higgins, S.-H. Park, P. J. King, C. J. Zhang, N. McEvoy, N. C. Berner, D. Daly, A. Shmeliov, U. Khan, G. Duesberg, V. Nicolosi and J. N. Coleman, *ACS Nano*, 2016, **10**, 3702–3713.
5 A. Franco Gonzalez, N.-H. Yang and R.-S. Liu, *J. Phys. Chem. C*, 2017, **121**, 27775–27787.
6 Y. Li, Q. Li, J. Chai, Y. Wang, J. Du, Z. Chen, Y. Rui, L. Jiang and B. Tang, *ACS Mater. Lett.*, 2023, **5**, 2948–2970.

7 H. Zhong, D. Liu, X. Yuan, X. Xiong and K. Han, *Energy Fuels*, 2024, **38**, 7693–7732.

8 K. Feng, M. Li, W. Liu, A. G. Kashkooli, X. Xiao, M. Cai and Z. Chen, *Small*, 2018, **14**, 1702737.

9 T. Shen, Z. Yao, X. Xia, X. Wang, C. Gu and J. Tu, *Adv. Eng. Mater.*, 2018, **20**, 1700591.

10 F. Holtstiege, A. Wilken, M. Winter and T. Placke, *Phys. Chem. Chem. Phys.*, 2017, **19**, 25905–25918.

11 Z. Xiao, C. Lei, C. Yu, X. Chen, Z. Zhu, H. Jiang and F. Wei, *Energy Storage Mater.*, 2020, **24**, 565–573.

12 A. Ulvestad, M. O. Skare, C. E. Foss, H. Krogsæter, J. F. Reichstein, T. J. Preston, J. P. Mæhlen, H. F. Andersen and A. Y. Koposov, *ACS Nano*, 2021, **15**, 16777–16787.

13 Y. Jin, B. Zhu, Z. Lu, N. Liu and J. Zhu, *Adv. Energy Mater.*, 2017, **7**, 1700715.

14 Z. Liu, Q. Yu, Y. Zhao, R. He, M. Xu, S. Feng, S. Li, L. Zhou and L. Mai, *Chem. Soc. Rev.*, 2019, **48**, 285–309.

15 A. N. Preman, H. Lee, J. Yoo, I. T. Kim, T. Saito and S.-k. Ahn, *J. Mater. Chem. A*, 2020, **8**, 25548–25570.

16 C. Zhu, K. Han, D. Geng, H. Ye and X. Meng, *Electrochim. Acta*, 2017, **251**, 710–728.

17 X. Lu, Y. Wang, X. Xu, B. Yan, T. Wu and L. Lu, *Adv. Energy Mater.*, 2023, **13**, 2301746.

18 G. G. Eshetu and E. Figgemeier, *ChemSusChem*, 2019, **12**, 2515–2539.

19 F. Boorboor Ajdari, P. Asghari, A. Molaei Aghdam, F. Abbasi, R. P. Rao, A. Abbasi, F. Ghasemi, S. Ramakrishna and N. Mikaeili Chahartagh, *Adv. Funct. Mater.*, 2024, **34**, 2314822.

20 S. He, S. Huang, X. Liu, X. Zeng, H. Chen, L. Zhao, H. Noor and X. Hou, *J. Colloid Interface Sci.*, 2024, **665**, 299–312.

21 C. E. L. Foss, M. K. Talkhoncheh, A. Ulvestad, H. F. Andersen, P. E. Vullum, N. P. Wagner, K. Friestad, A. Y. Koposov, A. van Duin and J. P. Mæhlen, *J. Phys. Chem. Lett.*, 2025, **16**, 2238–2244.

22 C. L. Berhaut, M. Mirolo, D. Z. Dominguez, I. Martens, S. Pouget, N. Herlin-Boime, M. Chandesris, S. Tardif, J. Drnec and S. Lyonnard, *Adv. Energy Mater.*, 2023, **13**, 2301874.

23 F. Fu, X. Wang, T. Hu, G. Zhou, F.-Z. Dai and S. Xu, *npj Comput. Mater.*, 2024, **10**, 131.

24 K. S. Chan, W.-W. Liang and C. K. Chan, *J. Phys. Chem. C*, 2019, **123**, 22775–22786.

25 B. Key, M. Morcrette, J.-M. Tarascon and C. P. Grey, *J. Am. Chem. Soc.*, 2011, **133**, 503–512.

26 J. Wang, L. Fan, Q. Du and K. Jiao, *Energy Adv.*, 2022, **1**, 269–276.

27 N. H. LaFemina, Q. Chen, R. H. Colby and K. T. Mueller, *J. Chem. Phys.*, 2016, **145**, 114903.

28 G. F. I. Toki, M. K. Hossain, W. U. Rehman, R. Z. A. Manj, L. Wang and J. Yang, *Ind. Chem. Mater.*, 2024, **2**, 226–269.

29 K. Hayamizu and Y. Aihara, *Electrochim. Acta*, 2004, **49**, 3397–3402.

30 D. Di Lecce, V. Marangon, H.-G. Jung, Y. Tominaga, S. Greenbaum and J. Hassoun, *Green Chem.*, 2022, **24**, 1021–1048.

31 T. P. Senftle, M. J. Janik and A. C. T. v. Duin, *J. Phys. Chem. C*, 2014, **118**, 4967–4981.

32 M. Raju, P. Ganesh, P. R. C. Kent and A. C. T. v. Duin, *J. Chem. Theory Comput.*, 2015, **11**, 2156–2166.

33 J. Wu, *Chem. Rev.*, 2022, **122**, 10821–10859.

34 A. P. Thompson, H. M. Aktulga, R. Berger, D. S. Bolintineanu, W. M. Brown, P. S. Crozier, P. J. in 't Veld, A. Kohlmeyer, S. G. Moore, T. D. Nguyen, R. Shan, M. J. Stevens, J. Tranchida, C. Trott and S. J. Plimpton, *Comp. Phys. Comm.*, 2022, **271**, 108171.

35 H. M. Aktulga, J. C. Fogarty, S. A. Pandit and A. Y. Grama, *Parallel Comput.*, 2012, **38**, 245–259.

36 Y. Liu, Q. Sun, P. Yu, Y. Wu, L. Xu, H. Yang, M. Xie, T. Cheng and W. A. I. Goddard, *J. Phys. Chem. Lett.*, 2021, **12**, 2922–2929.

37 A. Rahnamoun and A. C. T. van Duin, *J. Phys. Chem. A*, 2014, **118**, 2780–2787.

38 S. B. Olou'ou Guifo, J. E. Mueller, D. van Duin, M. K. Talkhoncheh, A. C. T. van Duin, D. Henriques and T. Markus, *J. Phys. Chem. C*, 2023, **127**, 2818–2834.

39 H. Park, A. C. T. v. Duin and A. Y. Koposov, *Chem. Mater.*, 2023, **35**, 2835–2845.

40 L.-T. Wu, E. K. W. Andersson, M. Hahlin, J. Mindemark, D. Brandell and J.-C. Jiang, *Sci. Rep.*, 2023, **13**, 9060.

41 K. Zhao, W. L. Wang, J. Gregoire, M. Pharr, Z. Suo, J. J. Vlassak and E. Kaxiras, *Nano Lett.*, 2011, **11**, 2962–2967.

42 H. Jung, M. Lee, B. C. Yeo, K.-R. Lee and S. S. Han, *J. Phys. Chem. C*, 2015, **119**, 3447–3455.

43 D. Kilymis, C. Gérard, J. Amodeo, U. Waghmare and L. Pizzagalli, *Acta Mater.*, 2018, **158**, 155–166.

44 S. Y. Lai, J. P. Mæhlen, T. J. Preston, M. O. Skare, M. U. Nagell, A. Ulvestad, D. Lemordant and A. Y. Koposov, *Nanoscale Adv.*, 2020, **2**, 5335–5342.

45 R. Pastore and G. Raos, *Soft Matter*, 2015, **11**, 8083–8091.

46 Z. Zheng, F. Li, J. Liu, R. Pastore, G. Raos, Y. Wu and L. Zhang, *Soft Matter*, 2018, **14**, 1219–1226.

47 V. A. Harmandaris, K. C. Daoulas and V. G. Mavrantzas, *Macromolecules*, 2005, **38**, 5796–5809.

48 Y. Yang, S. Wu, Y. Zhang, C. Liu, X. Wei, D. Luo and Z. Lin, *Chem. Eng. J.*, 2021, **406**, 126807.

49 J. Chen and S. Han, *Chem. Eng. J.*, 2023, **470**, 144150.

50 M. Bhati and T. P. Senftle, *J. Phys. Chem. C*, 2019, **123**, 27036–27047.

51 G. Yang, S. Frisco, R. Tao, N. Philip, T. H. Bennett, C. Stetson, J.-G. Zhang, S.-D. Han, G. Teeter, S. P. Harvey, Y. Zhang, G. M. Veith and J. Nanda, *ACS Energy Lett.*, 2021, **6**, 1684–1693.

52 B. Chen, Z. Zhang, M. Xiao, S. Wang, S. Huang, D. Han and Y. Meng, *ChemElectroChem*, 2024, **11**, e202300651.

53 J. W. Wang, Y. He, F. Fan, X. H. Liu, S. Xia, Y. Liu, C. T. Harris, H. Li, J. Y. Huang, S. X. Mao and T. Zhu, *Nano Lett.*, 2013, **13**, 709–715.

54 M. T. McDowell, S. W. Lee, J. T. Harris, B. A. Korgel, C. Wang, W. D. Nix and Y. Cui, *Nano Lett.*, 2013, **13**, 758–764.

55 X. H. Liu, J. W. Wang, S. Huang, F. Fan, X. Huang, Y. Liu, S. Krylyuk, J. Yoo, S. A. Dayeh, A. V. Davydov, S. X. Mao,

S. T. Picraux, S. Zhang, J. Li, T. Zhu and J. Y. Huang, *Nat. Nanotechnol.*, 2012, **7**, 749–756.

56 D. Diddens, W. A. Appiah, Y. Mabrouk, A. Heuer, T. Vegge and A. Bhowmik, *Adv. Mater. Interfaces*, 2022, **9**, 2101734.

57 S. Perez-Beltran, D. Kuai and P. B. Balbuena, *ACS Energy Lett.*, 2024, **9**, 5268–5278.

58 M. Kim, H. Moon, S. Kim, Y. Cho, T. Lee, S. Park, H. Kim, Y. H. Kwon, S. Hong and N.-S. Choi, *Chem. Eng. J.*, 2025, **511**, 162079.

59 S. Lei, Z. Zeng, M. Liu, H. Zhang, S. Cheng and J. Xie, *Nano Energy*, 2022, **98**, 107265.

60 N. Ding, J. Xu, Y. Yao, G. Wegner, X. Fang, C. Chen and I. Lieberwirth, *Solid State Ionics*, 2009, **180**, 222–225.

61 R. Ruffo, S. S. Hong, C. K. Chan, R. A. Huggins and Y. Cui, *J. Phys. Chem. C*, 2009, **113**, 11390–11398.

62 J. Xie, N. Imanishi, T. Zhang, A. Hirano, Y. Takeda and O. Yamamoto, *Mater. Chem. Phys.*, 2010, **120**, 421–425.

63 C. Park, M. Kanduč, R. Chudoba, A. Ronneburg, S. Risse, M. Ballauff and J. Dzubiella, *J. Power Sources*, 2018, **373**, 70–78.

64 M. Gu, Z. Wang, J. G. Connell, D. E. Perea, L. J. Lauhon, F. Gao and C. Wang, *ACS Nano*, 2013, **7**, 6303–6309.

65 M. J. Chon, V. A. Sethuraman, A. McCormick, V. Srinivasan and P. R. Guduru, *Phys. Rev. Lett.*, 2011, **107**, 045503.

66 M. K. Y. Chan, C. Wolverton and J. P. Greeley, *J. Am. Chem. Soc.*, 2012, **134**, 14362–14374.

67 N. He, H.-B. Xie and Y.-H. Ding, *J. Comput. Chem.*, 2008, **29**, 1850–1858.

68 K. Hankins, F. A. Soto and P. B. Balbuena, *J. Electrochem. Soc.*, 2017, **164**, E3457–E3464.

69 N. Artrith, A. Urban and G. Ceder, *J. Chem. Phys.*, 2018, **148**, 241711.

70 H. Kim, C.-Y. Chou, J. G. Ekerdt and G. S. Hwang, *J. Phys. Chem. C*, 2011, **115**, 2514–2521.

71 A. Stukowski, *Modell. Simul. Mater. Sci. Eng.*, 2009, **18**, 015012.